ANALYSIS OF STRONG GROUND MOTIONS FROM THE JUNE 12, 2005 ANZA EARTHQUAKE

Robert Graves, Paul Somerville, Nancy Collins, Arben Pitarka and Sidao Ni

URS Corporation
Pasadena, CA

Abstract

For shaking periods less than about 1 second, the observed ground motions from the 2005 Anza earthquake are significantly higher (around +1 sigma) than predicted by three recent NGA attenuation relations, with little systematic dependence on distance, Vs30 or Z2.5. This same trend is found comparing these data to motions computed from a broadband simulation technique. For shaking periods greater than about 1 second, both the empirical models and the numerical simulations do well at reproducing the median level of the data. We obtain a significant improvement in the fit to the shorter period motions by increasing the corner frequency in our broadband simulation by a factor of 1.6. These results suggest that the strong short period motions resulted from a rupture process having a relatively high dynamic stress drop.

Introduction

The Anza earthquake occurred on June 12, 2005 at 08:41:46 PDT. Preliminary analysis placed the event at lon=-116.57 and lat=33.53 with a hypocentral depth of 14.2 km and a magnitude of 5.1 (see http://earthquake.usgs.gov/eqcenter/shakemaps/sc/shake/14151344). Several sites in the epicentral region recorded peak ground accelerations (PGA) exceeding 0.2 g, producing areas of instrumental intensity approaching level VI (moderate to strong perceived shaking). The earthquake occurred along the San Jacinto fault zone just south of the Anza "seismic gap" (Figure 1). The occurrence of this earthquake in close proximity to a major active fault, as well as the relatively high ground motions produced during the rupture, has potentially significant implications for seismic hazards in southern California.

In this paper, we analyze the recorded ground motions to investigate the influence of source, path and site effects on the level and pattern of observed strong motions. Our goals are to better understand the processes that control the generation of strong ground motion and to investigate the ability of empirical ground motion models and numerical simulation methods to reproduce the observations. We find that the Anza earthquake produced relatively high short period ground motions independent of propagation distance and site type. This suggests that the earthquake source was the main contributor to the elevated short period motions through a high dynamic stress drop. In the sections that follow, we first discuss the recorded strong motion data and provide comparisons of these data with recently published ground motion attenuation models. Next, we compare the recorded motions with simulated broadband (0-10 Hz) motions

and demonstrate that we are able to improve the modeling of short period motions by a simple increase in the source corner frequency.

Recorded Ground Motions

A large number of strong ground motion records were obtained during this earthquake. Table 1 lists the organizations and numbers of stations recording the event in the southern California region for which we have obtained waveform data.

Table 1: Ground Motion Recordings.

Organization	Instrument Type	Number of Recordings
ANZA Array	broadband	12
CSMIP	strong motion	90
SCSN/TriNet	broadband	178
USGS/NSMP	strong motion	19

A map of free field strong motion recording stations is shown in Figure 2. We obtained the uncorrected strong motion waveform data and then applied baseline and filtering operators to correct these data. The usable bandwidth is 0.2 to 40 Hz. Then we processed the corrected data to extract peak acceleration (PGA) and peak velocity (PGV) values, as well as computing spectral acceleration (SA) values at a variety of periods.

Although most of the near source broadband recordings were clipped, the more distant broadband records, which are not clipped, are useful in constraining the source mechanism. To do this, we use both a moment-tensor (MT) inversion and a cut-and-paste (CAP) inversion (Zhu and Helmberger, 1996). The MT inversion uses long period (T > 14 sec) regional surface waves to determine the best fitting moment tensor solution. The CAP inversion uses both long period (T > 10 sec) regional waveforms as well as shorter period (T > 3 sec) Pnl waveforms to find the best fitting double couple solution. For this earthquake, both methods give very similar results, indicating primarily strike slip faulting along steeply dipping planes. The nodal planes are roughly parallel and conjugate to the San Jacinto fault. Table 2 summarizes these best fitting solutions.

T**able 2:** Inverted Source Mechanisms.

	MT Inversion	CAP Inversion
Strike	303	302
Dip	61	60
Rake	178	177
Depth (km)	14	14
M_w	5.12	5.08

Comparison of Recorded Motions with NGA Models

As a first step in our analysis, we compare the recorded motions against the recently developed NGA ground motion relations of Campbell and Bozorgnia (2007), Chiou and Youngs (2006) and Boore and Atkinson (2007). The earthquake is parameterized as a strike-slip event

with a depth of 14 km and a moment magnitude of 5.1. Figure 3 plots PGA as a function of distance. We determine site Vs30 values using the map of Wills et al. (2000). For this comparison, the data are grouped into sites with Vs30 < 450 m/s and sites with Vs30 > 450 m/s, and then we use reference Vs30 values of 300 m/s and 700 m/s, respectively, in the ground motion models. For both Vs30 groups, the PGA values for the Anza earthquake are significantly higher than predicted by the models, clustering around the +1 sigma level across a broad distance range.

Figure 4 compares 1 second SA computed from the recorded waveforms against that predicted by the three NGA relations. The same reference Vs30 values are used as in Figure 3. For this longer period level, the ground motion models are much closer to the median level of the ground motions across the entire distance range.

We also compare the data and NGA relations using goodness-of-fit measures for 5% damped spectral acceleration calculated from the broadband time histories (e.g., Abrahamson, et al., 1990). For an individual station, the residual $r(T_i)$ at each period T_i is given by $r(T_i) = \ln[sa_O(T_i)/sa_M(T_i)]$, where $sa_O(T_i)$ and $sa_M(T_i)$ are the observed and model predicted spectral acceleration values, respectively. To calculate the model predictions, we use site specific Vs30 and Z2.5 (depth to Vs=2.5 km/s) values for each of the stations. The model bias is obtained by averaging the residuals for all stations and both horizontal components at each period. A model bias of zero indicates the model, on average, matches the observed ground motion level. A negative model bias indicates over-prediction and a positive model bias indicates under-prediction of the observations. The results for the three NGA models are shown in Figure 5. All three models have little systematic bias for periods greater than about 1 second, with a standard error of about 0.5 (natural log units). For periods below about 1 second, the models begin to under-predict the data, with a bias that approaches 0.9 in natural log units (factor of 2.5) at a period of about 0.1 second.

Figures 6, 7, and 8 examine these residuals as a function of closest distance, Vs30 and Z2.5, respectively. In order to investigate possible azimuthal variations, in each of these figures we have also divided the stations into four quadrants (northeast, southeast, southwest and northwest) relative to the epicenter location. The stations for each quadrant are indicated by a different color/symbol combination in these figures. Finally, each figure shows results for four ground motion metrics: PGA, SA at 0.3 seconds, SA at 1.0 seconds, and SA at 3.0 seconds. The strongest trend seen in these figures is the significant under-prediction of the data by all of the models at the shorter periods. Aside from the slight trend of increasing residual with increasing distance particularly at 0.3 second SA (Figure 6), we do not see any significant correlation of the residuals with either distance, Vs30 or Z2.5.

The results shown in Figures 3 through 8 suggest that the elevated level of short period motions may have resulted from a source effect, rather than path and/or site effects. That is, the source process appears to have had very strong high frequency radiation, due for example, to high dynamic stress drop.

Broadband Ground Motion Simulations

To further investigate the relative contributions of source, path and site effects on the motions, we utilize numerical ground motion simulations. In our approach, the broadband ground motion simulation procedure is a hybrid technique that computes the short period and long period ranges separately and then combines the two to produce a single time history (Graves and Pitarka, 2004). At periods greater than 1 second, the methodology is deterministic and contains a theoretically rigorous representation of kinematic fault rupture and wave propagation effects in 3D viscoelastic media. For this study we derive the 3D velocity structure from the SCEC CVM (version 4). We set the minimum shear velocity at 620 m/s and use a grid spacing of 125 m in the finite-difference grid. Over 500 million nodes are required to represent the model, and the calculation was performed on the Linux cluster at USC's center for High Performance Computing and Communications.

The short-period (T < 1 sec) simulation methodology computes the response assuming a random phase, an omega-squared source spectrum, and simplified Green's functions. The methodology follows from Boore (1983) with the extension to finite-faults given by Frankel (1995) and Hartzell et al. (1999). The source is represented by one or more subfaults, each of which rupture with a moment proportional to the final slip given by the original source model. The subfault moment values are scaled uniformly so that the total moment matches that of the original source model. The subfault corner frequency (f_c) is defined by

$$f_c = s_z s_t \frac{v_r}{\pi d} \tag{1}$$

where v_r is the rupture speed, d is the subfault dimension, s_z scales the corner frequency with depth, and s_t relates the corner frequency to the rise time of the subfault source. In our methodology, we use a uniform value of $s_t = 1.6$. From the surface to a depth of 5 km, the depth scaling factor is set to a constant value, $s_z = 1.0$. This value increases linearly with depth to a value of $s_z = 1.4$ at 10 km. Below 10 km depth, s_z is constant at 1.4. This parameterization follows from the observation in crustal earthquakes that slip rate is relatively low for shallow ruptures and increases with rupture depth (Kagawa et al., 2004). Because corner frequency scales with slip rate, this formulation replicates the trend of the observations. We note that although this formulation reduces the number of free parameters, it is not unique and probably has tradeoffs with other parameters in the stochastic model. In particular, allowing the subfault stress parameters to vary across the fault would accommodate a similar slip rate scaling. Instead, we fix the stress parameter to a uniform value of 50 in our simulations. Finally, the convolution operator of Frankel (1995) scales the subevent corner frequency to the corner frequency of the target event.

The formulation requires the specification of a 1D layered velocity model in calculating simplified Green's functions and impedance effects. In this study, we use a 1D velocity model that roughly follows the average depth variations in the 3D structure, and we include both direct and Moho-reflected rays, which are attenuated by $1/R_p$, where R_p is the total path length traveled by the particular ray. For each ray we compute a radiation pattern coefficient by averaging over a range of slip mechanisms and take-off angles. Anelasticity is incorporated via a travel time

weighted average of the Q values for each of the material layers and a generic rock site spectral decay operator, $\kappa = 0.05$. Finally, gross impedance effects are included using quarter wavelength theory (Boore and Joyner, 1997) to derive amplification functions that are consistent with the specified 1D velocity structure.

To account for site specific geologic conditions in both the short and long period simulations, we apply period dependent, non-linear amplification functions to the simulated time histories. These functions were derived empirically by Borcherdt (1994) and have the general form

$$F_x = \left(\frac{v_{site}}{v_{ref}} \right)^{m_x} \tag{2}$$

where v_{site} denotes the 30 m travel-time averaged shear wave speed (Vs30) at the site of interest, v_{ref} corresponds to the Vs30 where the ground response is known, and m_x denotes an empirically determined factor that depends on both period and ground motion level. For each location in the simulation grid, we obtain the site specific Vs30 (v_{site}) from the map of Wills et al. (2000) and v_{ref} is set to the shear wave speed from the 3D velocity model for that location.

For the Anza earthquake, we define a fault plane having a total area of 13 km^2 (3.6 km by 3.6 km), consistent with the scaling relation of Somerville et al (1999). The fault depth is 14 km and the orientation of the plane and sense of slip are given by the CAP inversion results in Table 2 with the moment set at 5 x 10^{23} dyne-cm. The region covered by the simulation included 79 sites which recorded the Anza earthquake, extending to epicentral distances of about 110 km. Most of the stations not included in this region are southwest of the epicenter in the San Diego area (see Figure 2). For the long period simulation, the source is represented as a point moment-tensor within the finite-difference grid. The deterministic slip function is a triangle having a rise time of 0.2 seconds, which is well below the deterministic bandwidth threshold of 1 second. For the short period simulation, we use 1 subfault to represent the source, which has a resulting corner frequency of 1.3 Hz after application of the Frankel convolution operator. Based on the analysis of the simulation results obtained with the above parameterization (described below), we have also run the short period model using a corner frequency scaled by an additional factor of 1.6, giving f_c = 2 Hz.

Figure 9 compares the model bias and goodness-of-fit results between the simulated and recorded spectral accelerations at 79 sites. The top panel of this figure shows the results from the original simulation and the bottom panel shows the results obtained with the additional scaling of corner frequency. The original simulation (f_c = 1.3 Hz) produces results that are quite similar to the goodness-of-fit results obtained with the empirical ground motion models (Figure 5). That is, at long periods (T > 1 sec), the simulation has little bias and a standard error of about 0.5 (natural log units). At short periods, this simulation significantly under-predicts the observed motions in a manner very similar to the empirical models. However, the refined simulation (f_c = 2 Hz) produces a much better match to the observed motions at the shorter periods.

We provide a detailed examination of these residuals in Figures 10, 11 and 12, which plot the results as a function of closest distance, Vs30, and Z2.5, respectively. As was done in the earlier comparisons with the empirical models, we group the stations by quadrant, although, as was mentioned previously, the simulation grid has relatively few sites in the southwest quadrant (blue circles in the figures). These figures show a very clear and systematic difference in the two simulation results. The scaling of corner frequency in the refined simulation produces a much improved fit to the shorter period observations compared to the original simulation. Comparing these results with the results from the empirical ground motion models (Figures 6, 7 and 8), we see that the behavior of the original simulation is quite similar to the empirical models. Again, aside from the slight trend of increasing residual with increasing distance particularly at 0.3 second SA (Figure 10), we do not see any significant correlation of the simulation residuals with either distance, Vs30 or Z2.5.

One of the benefits of the numerical simulation approach is that it produces full three component time histories for each site. Figure 13 compares recorded and simulated (fc = 2 Hz) ground velocity waveforms at 18 selected sites. For this comparison, we have bandpass filtered both the data and synthetics in the period range $1 < T < 5$ seconds, in order to concentrate on the more deterministic features of the waveforms. The distance range of the sites shown in Figure 13 spans from 18 to 119 km. For the stations nearest the epicenter, both the recorded and simulated motions are relatively brief. As the distance range increases, the recorded motions begin to show more complexity and significantly longer durations of shaking. In general, the waveforms and amplitudes of the main S-wave pulses are matched reasonably well by the simulations. The match of the synthetics to the data clearly exhibits significant variability among these sites, with some sites being matched quite well (e.g., 13162), and other sites not matched nearly as well (e.g., 12092). We attribute these differences primarily to limitations of the current 3D velocity model used in the simulations.

Discussion and Conclusions

The comparisons presented in the preceding sections suggest that the 2005 Anza earthquake had a source process that radiated relatively strong short period energy. The success of the numerical modeling using the scaled-up corner frequency further suggests that the increase in short period radiation is related to the dynamics of rupture. One potential mechanism to produce this effect is a relatively high slip velocity possibly in conjunction with a fast rupture across a concentrated high slip patch on the fault. Either of these can produce a relatively high dynamic stress drop during rupture, which will result in elevated levels of shorter period radiation. Unfortunately, the current resolution of our numerical modeling doesn't allow discrimination between these effects. Further study aimed at mapping out the finer scale details of the rupture process are needed to address these questions. These studies might include examination of pre- and post-event seismicity to characterize the spatial and temporal evolution of these ruptures with the aim of constraining the mainshock rupture area. Additionally, analysis of short period directivity effects may also provide constraints on the nature and orientation of rupture (Tan and Helmberger, 2007).

On a broader scale, the features of this earthquake are certainly indicative of the state of stress along this section of the San Jacinto fault zone, with possible implications for seismic

hazard mitigation. The Anza region has several conjugate structures intersecting the San Jacinto fault zone (Tom Rockwell, personal communication). The apparent high dynamic stress drop of the 2005 event is suggestive of rupture on a less well developed conjugate structure. If the 2005 event (and previous events such as 2001) occurred along one of these conjugate structures, then it may suggest that the through-going fault structure (San Jacinto fault) is moving closer to failure. Rockwell has documented numerous M ~ 7 paleo-earthquakes at a site about 10 km northwest of the 2005 event (Hog Lake, just across the seismic gap). Clearly, the main fault trace is active and capable of generating significant earthquakes. Further study of the Anza earthquake may provide valuable insight into the seismogenic process of the San Jacinto fault zone.

Acknowledgements

Strong ground motion recordings from the US Geological Survey and the Strong Motion Instrumentation Program (SMIP) of the California Geological Survey provided the bulk of the data used in this study. The large scale 3D numerical calculations were carried out on the Linux cluster at USC's center for High Performance Computing and Communications under a grant to the Southern California Earthquake Center. Funding for this work was provided by the Data Interpretation Project of the California Strong Motion Instrumentation Program.

References

Abrahamson, N. A., P. G. Somerville, and C. A. Cornell (1990). Uncertainty in numerical strong motion predictions, *Proc. 4th U.S. National Conf. on Earthquake Engineering*, **1**, 407-416.

Boore, D. M. (1983). Stochastic simulation of high-frequency ground motions based on seismological models of the radiated spectra. *Bull. Seism. Soc. Am.*, **73**, 1865–1894.

Boore, D. M. and W. B. Joyner (1997). Site amplifications for generic rock sites. *Bull. Seism. Soc. Am.*, **87**, 327–341.

Boore, D. and G. Atkinson (2007). Boore-Atkinson NGA ground motion relations for the geometric mean horizontal component of peak and spectral ground motion parameters, *Technical Report 2007/01, Pacific Earthquake Engineering Research Center,* University of California, Berkeley, CA.

Borcherdt, R. D. (1994). Estimates of site-dependent response spectra for design (methodology and justification). *EQ Spectra*, **10**, 617–653.

Campbell, K.W. and Y. Bozorgnia (2007). Campbell-Bozorgnia NGA ground motion relations for the geometric mean horizontal component of peak and spectral ground motion parameters, *Technical Report 2007/02, Pacific Earthquake Engineering Research Center,* University of California, Berkeley, CA.

Chiou, B. S. J. and R. R. Youngs (2006). Chiou and Youngs PEER-NGA empirical ground motion model for the average horizontal component of peak acceleration and pseudo-spectral acceleration for spectral periods of 0.01 to 10 seconds, *Interim Report for USGS Review, Pacific Earthquake Engineering Research Center*, University of California, Berkeley, CA.

Frankel, A. (1995). Simulating strong motions of large earthquakes using recordings of small earthquakes: the Loma Prieta mainshock as a test case. *Bull. Seism. Soc. Am.*, **85**, 1144–1160.

Graves, R. W. and A. Pitarka (2004). Broadband time history simulation using a hybrid approach, *Proc. 13th World Conference on Earthquake Engineering*, Vancouver, Canada. paper no. 1098.

Hartzell, S., S. Harmsen, A. Frankel, and S. Larsen (1999). Calculation of broadband time histories of ground motion: Comparison of methods and validation using strong-ground motion from the 1994 Northridge earthquake, *Bull. Seism. Soc. Am.*, **89**, 1484–1504.

Kagawa, T., K. Irikira, and P. G. Somerville (2004). Differences in ground motion and fault rupture process between the surface and buried rupture earthquakes, *Earth, Planets, and Space*, **56**, 3–14.

Lin, G., P. M. Shearer, and E. Hauksson (2007). Applying a 3D velocity model, waveform cross-correlation, and cluster analysis to locate southern California seismicity from 1981 to 2005, s*ubmitted to J. Geophys. Res.*

Somerville, P. G., K. Irikura, R. Graves, S. Sawada, D. Wald, N. Abrahamson, Y. Iwasaki, T. Kagawa, N. Smith, and A. Kowada (1999). Characterizing crustal earthquake slip models for the prediction of strong ground motion, *Seism. Res. Lett*., **70**(1), 199–222.

Tan, Y., and D. Helmberger (2007). Rupture directivity of the 2003 Big Bear aftershocks, *submitted to Bull. Seism. Soc. Am.*

Wills C, M. Petersen, W. Bryant, M. Reichle, G. Saucedo, S. Tan, G. Taylor and J. Treiman (2000). A site conditions map for California based on geology and shear wave velocity. *Bull. Seism. Soc. Am.*, **90**(6B): S187-S208.

Zhu, L. and D. Helmberger (1996). Advancement in source estimation techniques using broadband regional seismograms, *Bull. Seism. Soc. Am.*, **86**, 1634-1641.

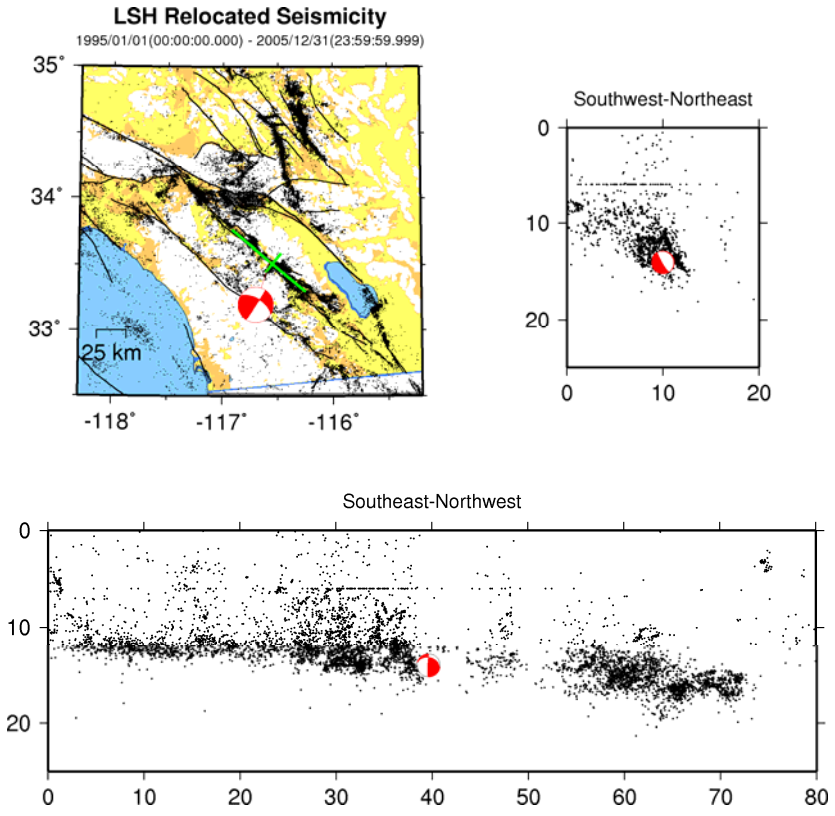

Figure 1: Relocated seismicity of southern California from 1995 through 2005 (Lin et al., 2007). The 2005 Anza event is indicated by "beach ball" mechanism. The event occurred at the southern edge of the Anza seismic gap at a depth of about 14 km. The mechanism is primarily strike slip, although the exact fault plane is ambiguous.

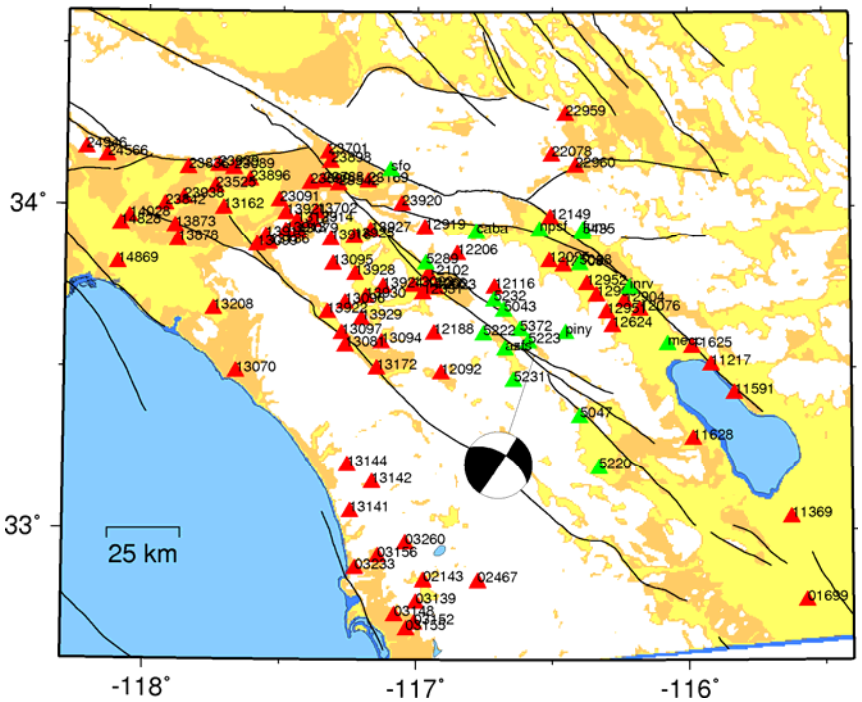

Figure 2: Map showing strong motion recording sites for the 2005 Anza earthquake. Green triangles are stations operated by the USGS and red triangles are CGS stations.

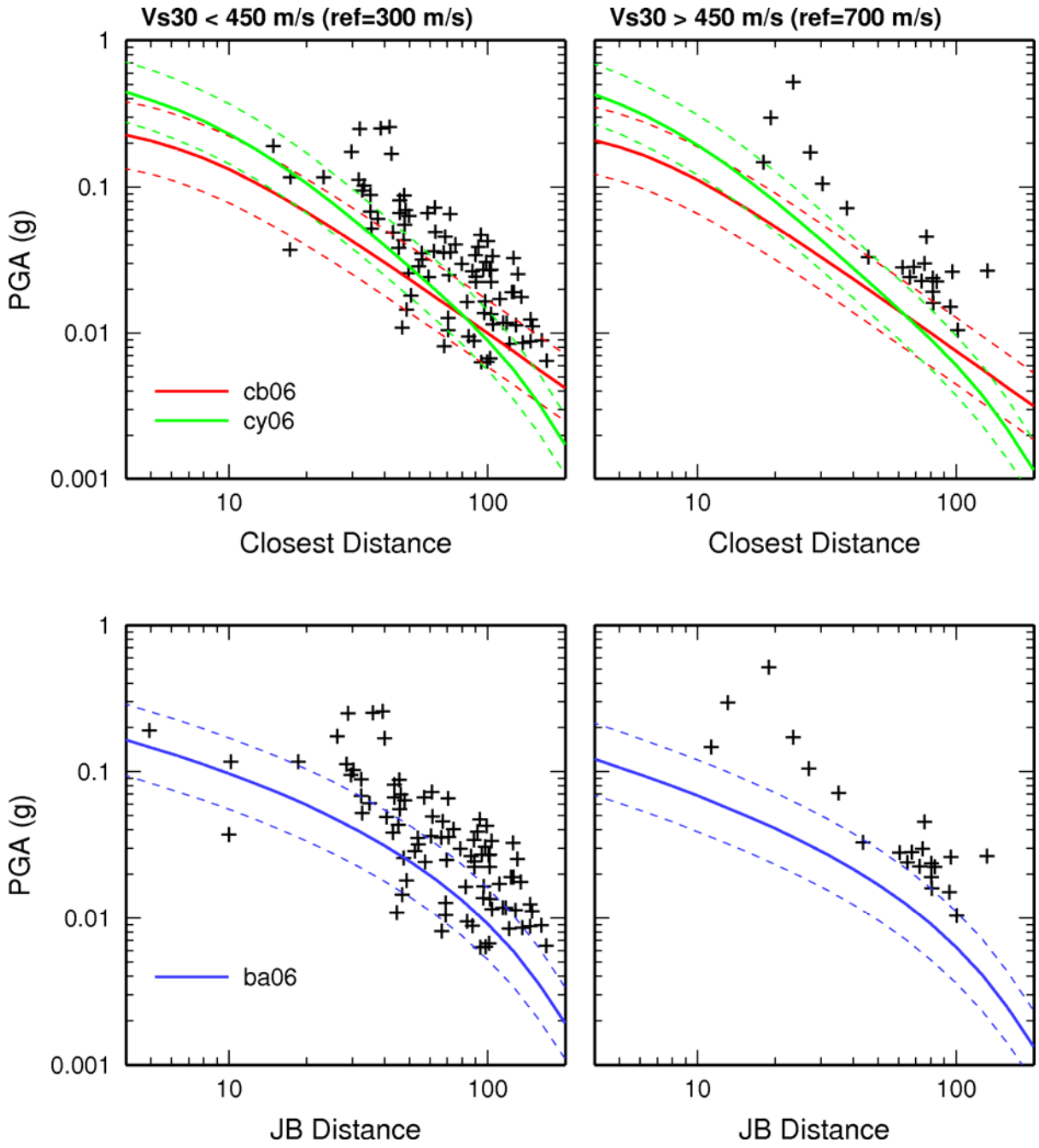

Figure 3: Attenuation of peak ground acceleration (PGA) as a function of distance for the Anza earthquake. Closest distance is used in the top panels and Joyner-Boore distance is used in the bottom panels. Median (solid lines) and +/- 1 sigma (dashed lines) attenuation curves from three recent NGA ground motion models are shown as well (cb06 is Campbell and Bozorgnia, 2006; cy06 is Chiou and Youngs, 2006; ba06 is Boore and Atkinson, 2006). The left panels show data from sites having Vs30 less than 450 m/s and the right panels show data for site with Vs30 greater than 450 m/s. Reference Vs30 values used in the empirical models are 300 m/s and 700 m/s for the left and right panels, respectively.

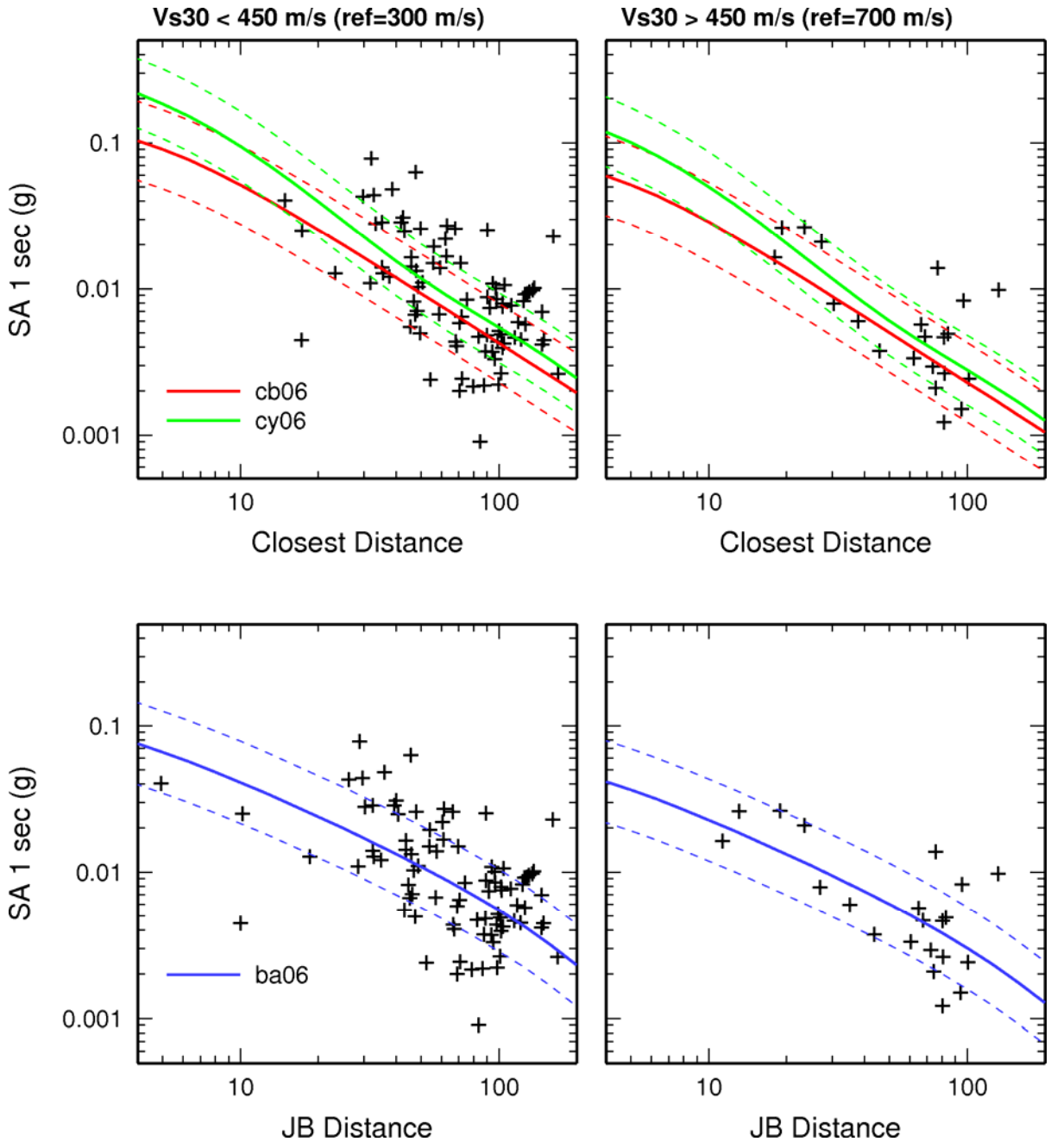

Figure 4: Same as Figure 3 except ground motion parameter is spectral acceleration (SA) at 1 second period.

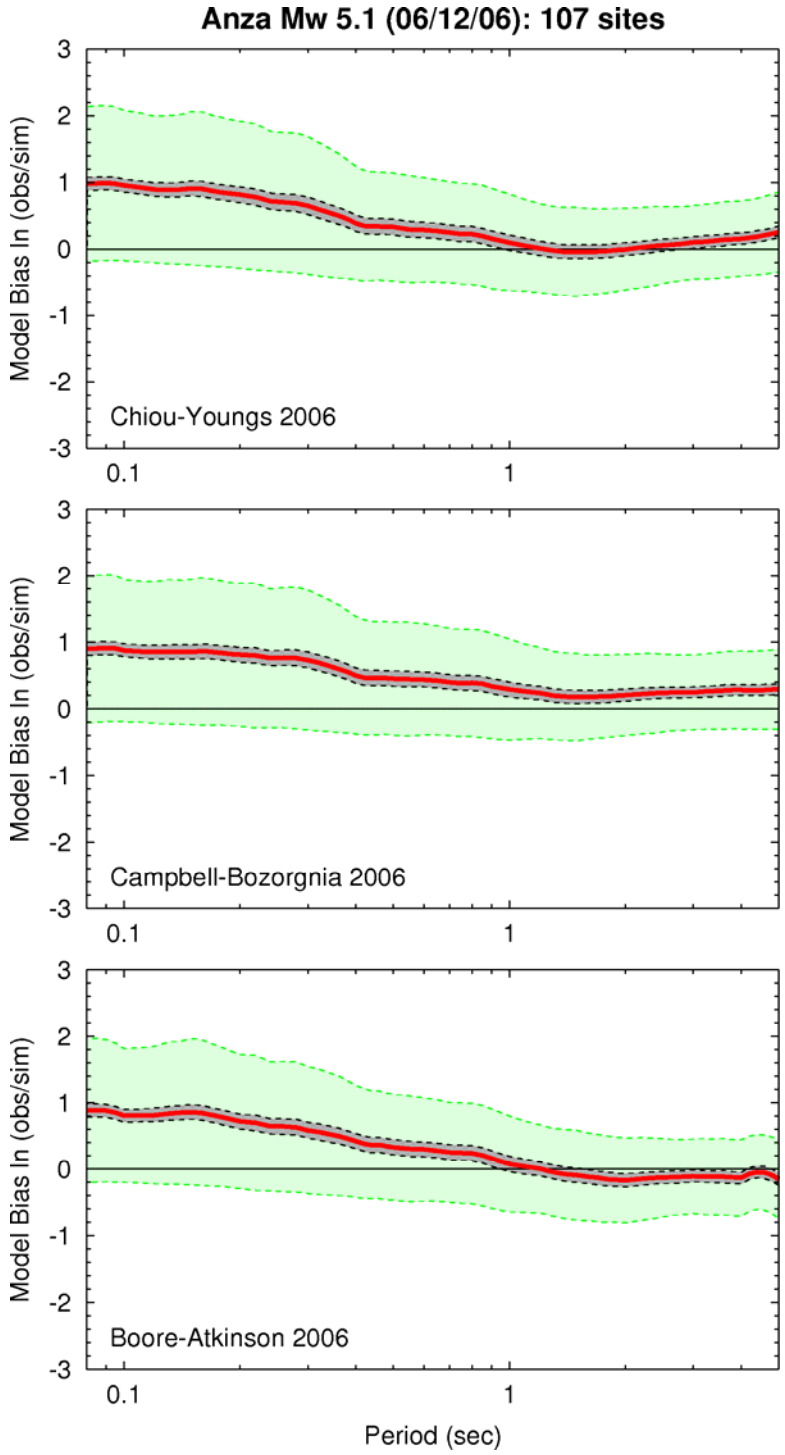

Figure 5: Model bias and goodness-of-fit for the three NGA ground motions models for the Anza earthquake data. Ground motions from total of 107 stations are used for this analysis. The heavy red line is the overall model bias, the green shading represents +/- 1 sigma, and the grey shading is the 90% confidence of the mean. All three models produce quite similar results, with a significant under-prediction of the data for periods less than about 1 second.

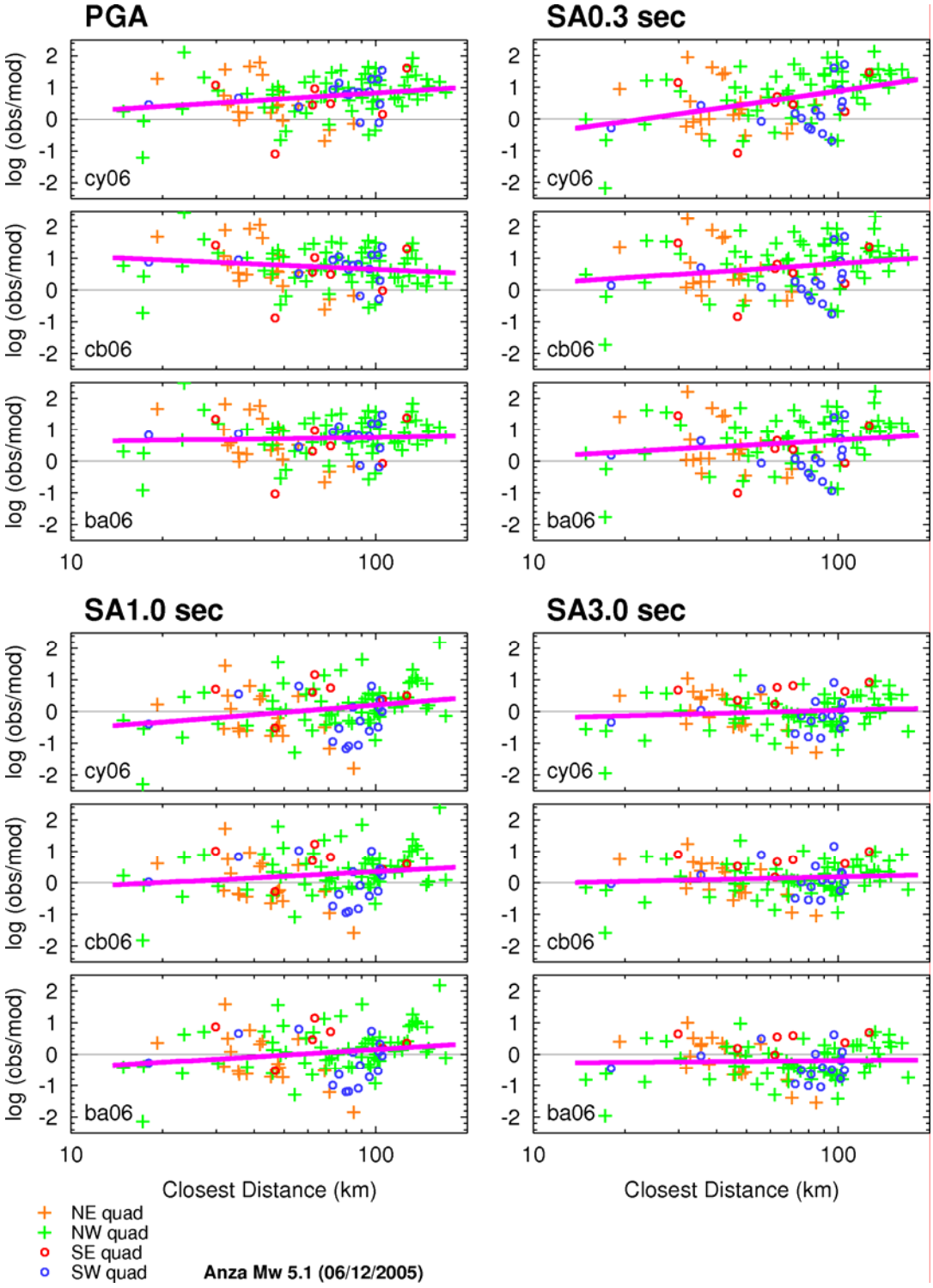

Figure 6: Residuals between observed ground motion values and the three NGA model predictions plotted as a function of closest distance to rupture. Each set of three panels shows results for a different ground motion metric: PGA in upper left, SA at 0.3 seconds in upper right, SA at 1.0 second in lower left, and SA at 3.0 seconds in lower right. Site locations are grouped into four quadrants relative to the epicenter, as denoted by the different colored symbols. The heavy line on each panel is a least square fit to the residuals. There is a clear trend of increasing under-prediction with decreasing period for all models.

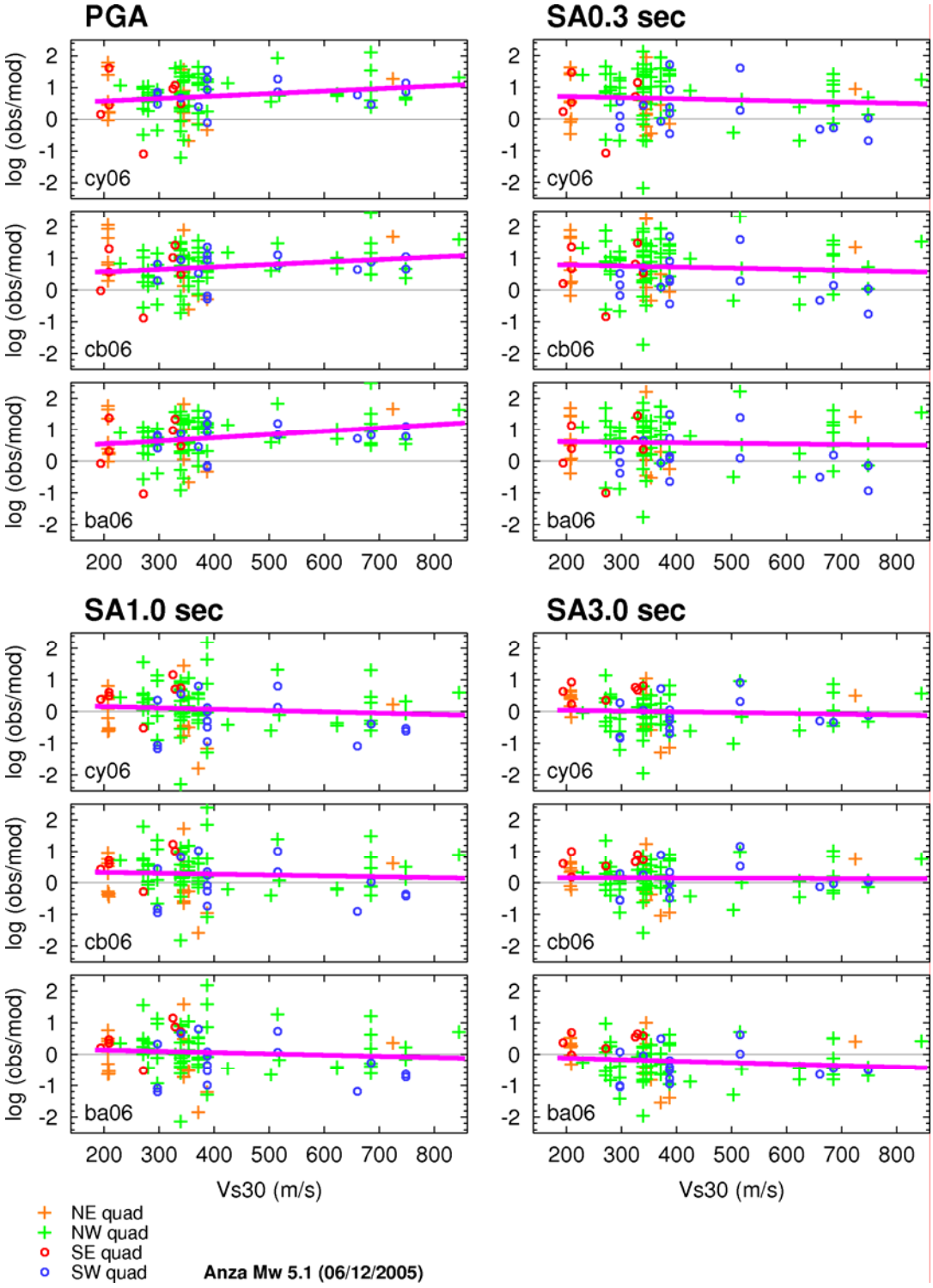

Figure 7: Same as Figure 6 except residuals are plotted as a function of Vs30 value.

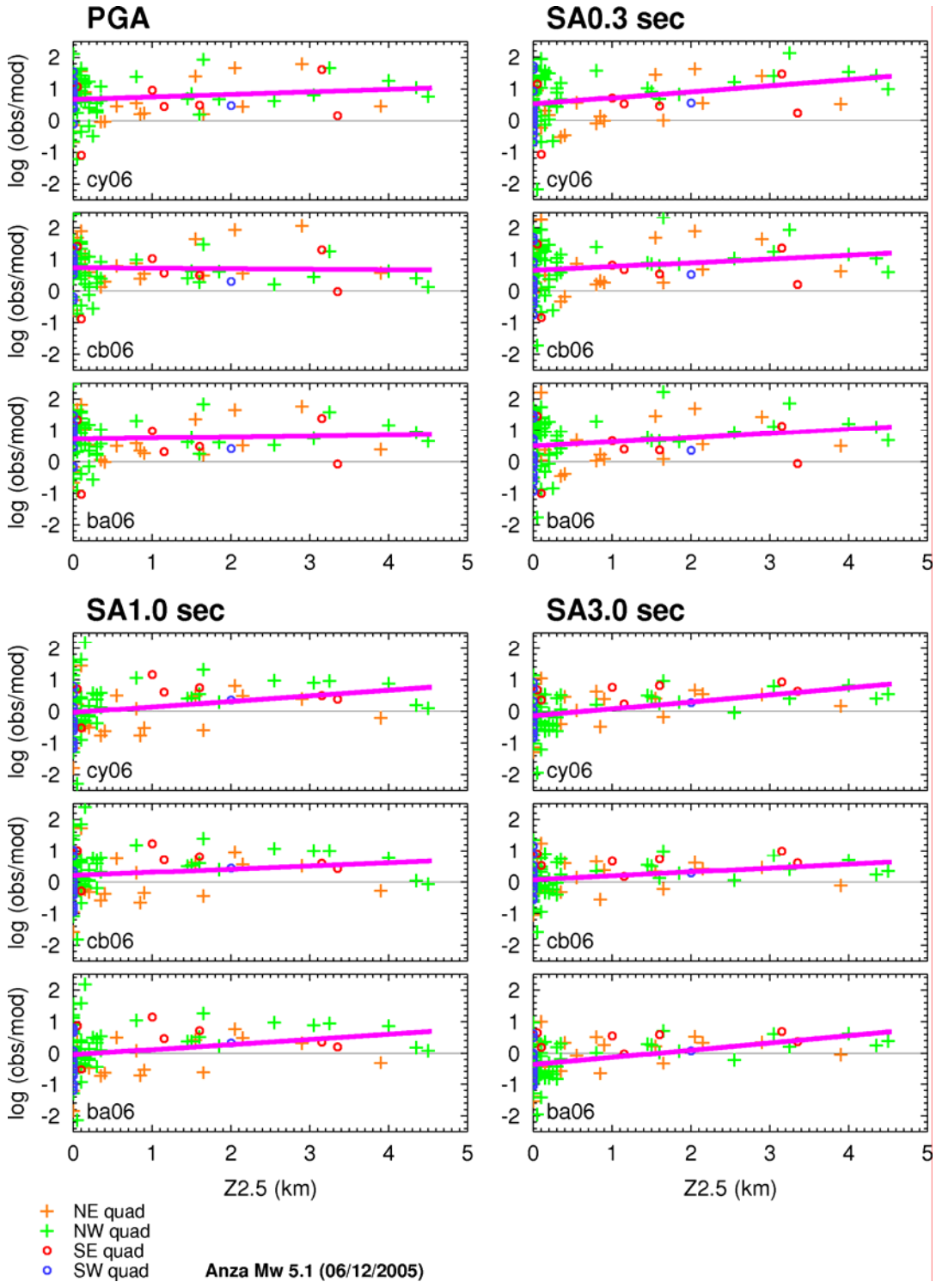

Figure 8: Same as Figure 6 except residuals are plotted as a function of depth to Vs=2.5 km/s isosurface (Z2.5).

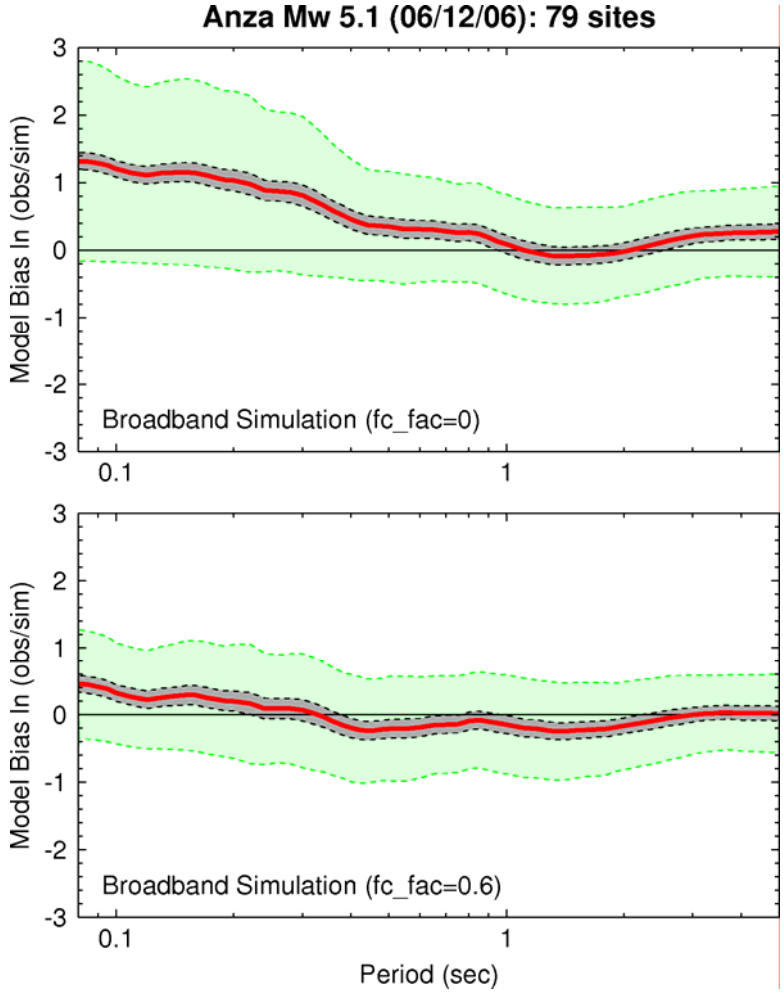

Figure 9: Model bias and goodness-of-fit for the numerical ground motion simulations for the Anza earthquake data. Ground motions from total of 79 stations are used for this analysis. The heavy red line is the overall model bias, the green shading represents +/- 1 sigma, and the grey shading is the 90% confidence of the mean. The top panel shows results using a generic source description and is quite similar to the empirical models, with a significant under-prediction of the data for periods less than about 1 second. The bottom panel shows results for a simulation using a 60% increase in the source corner frequency, which produces a much better match to the observations.

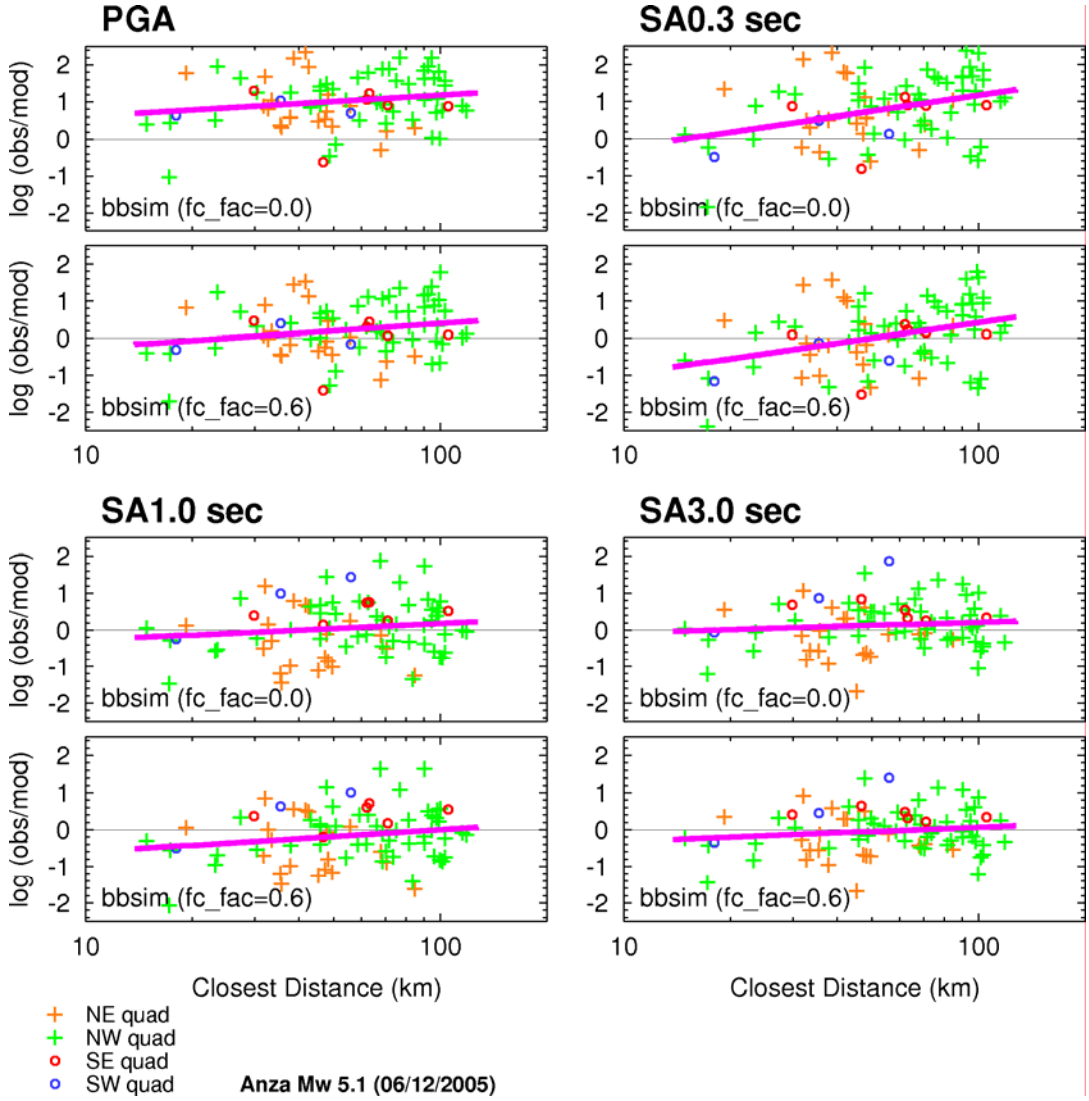

Figure 10: Residuals between observed ground motion values and the two broadband ground motion simulations plotted as a function of closest distance to rupture. The top panel in each group shows results using a generic source corner frequency and the bottom panel shows results for a simulation using a 60% increase in the source corner frequency. Each set of two panels shows results for a different ground motion metric: PGA in upper left, SA at 0.3 seconds in upper right, SA at 1.0 second in lower left, and SA at 3.0 seconds in lower right. Site locations are grouped into four quadrants relative to the epicenter, as denoted by the different colored symbols. The heavy line on each panel is a least square fit to the residuals. The first simulation shows a clear trend of increasing under-prediction with decreasing period, similar to the empirical models, whereas the second simulation produces a significantly better fit to the data.

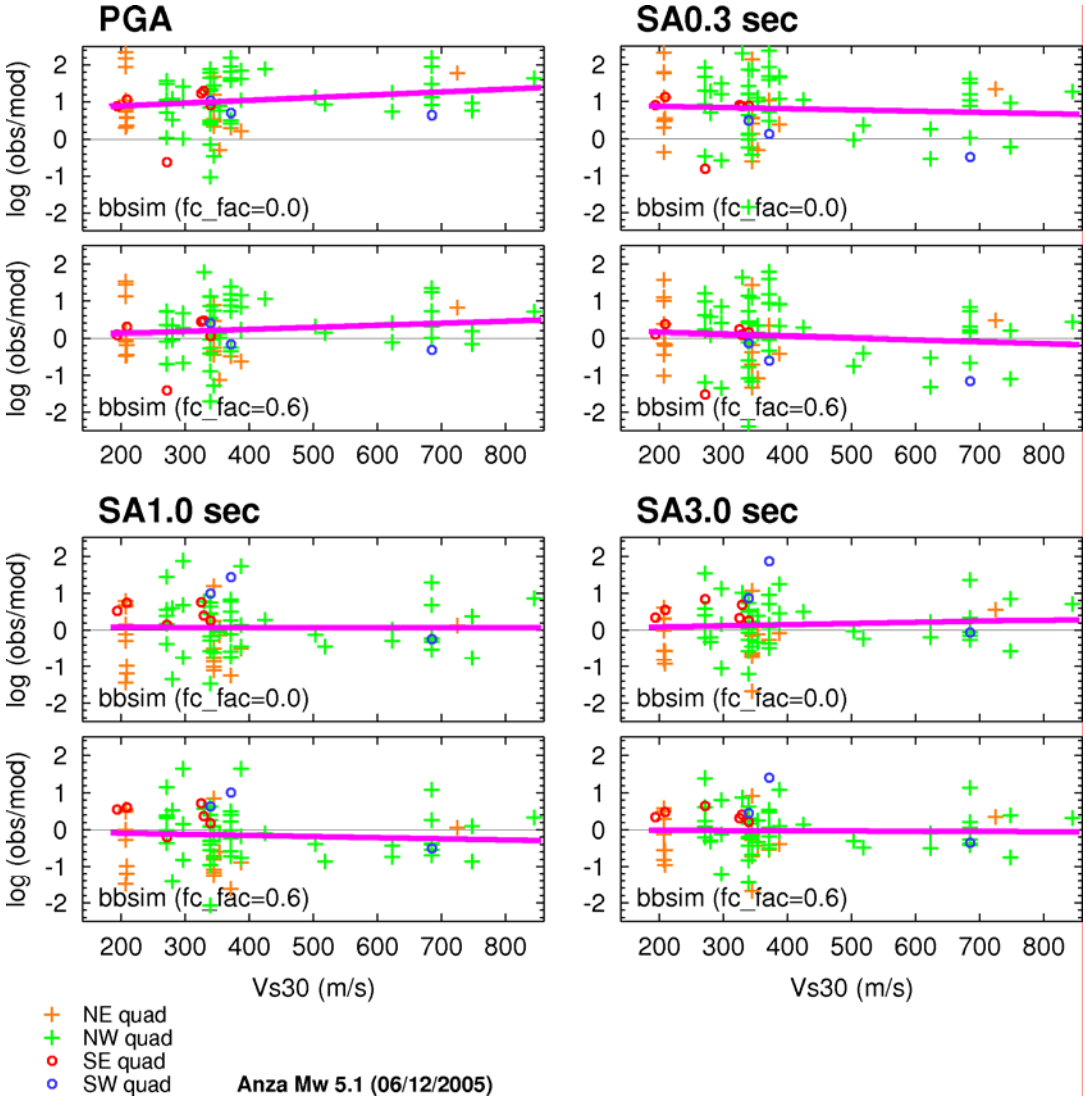

Figure 11: Same as Figure 10 except residuals are plotted as a function of Vs30 value.

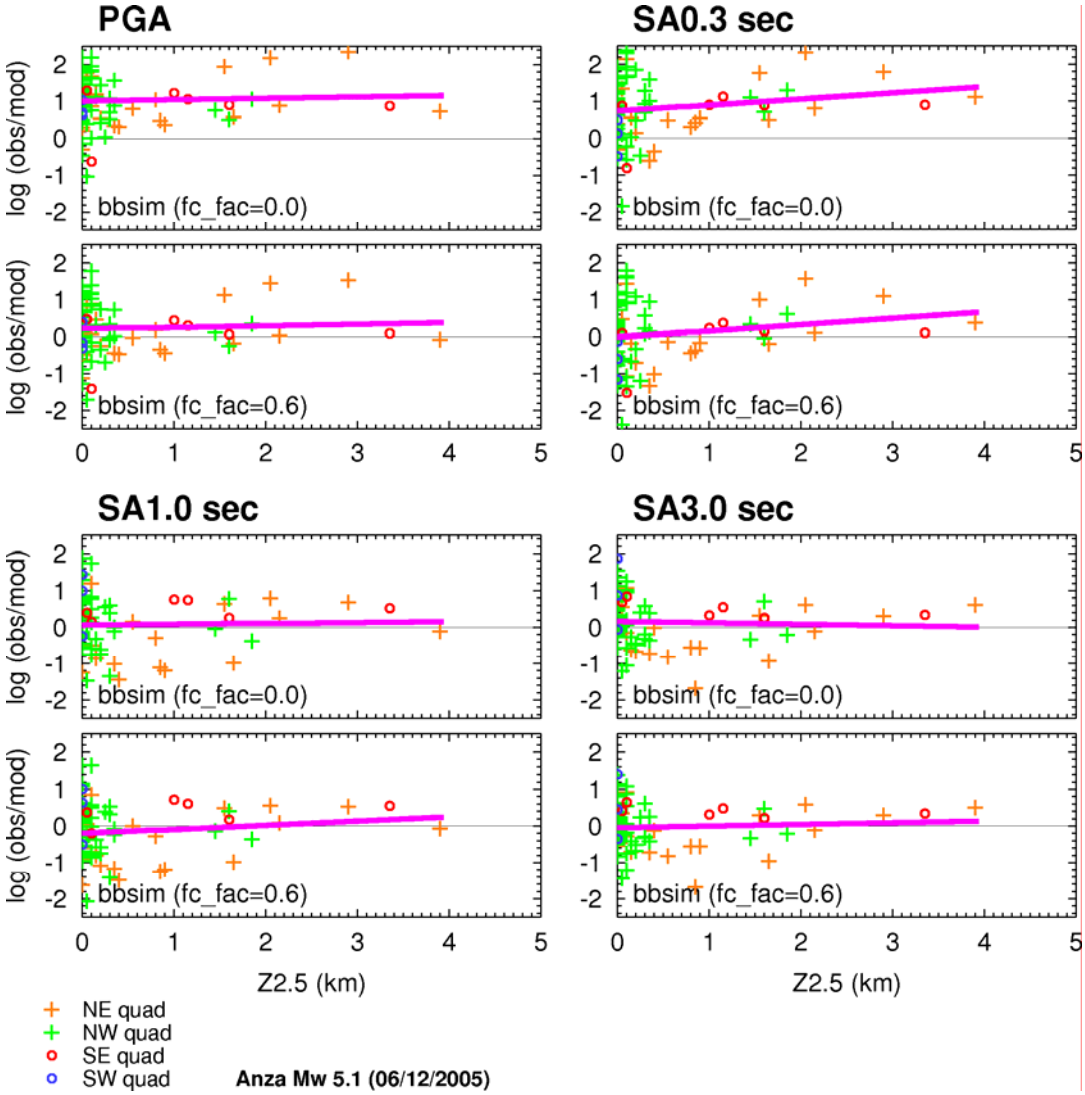

Figure 12: Same as Figure 10 except residuals are plotted as a function of depth to Vs=2.5 km/s isosurface (Z2.5).

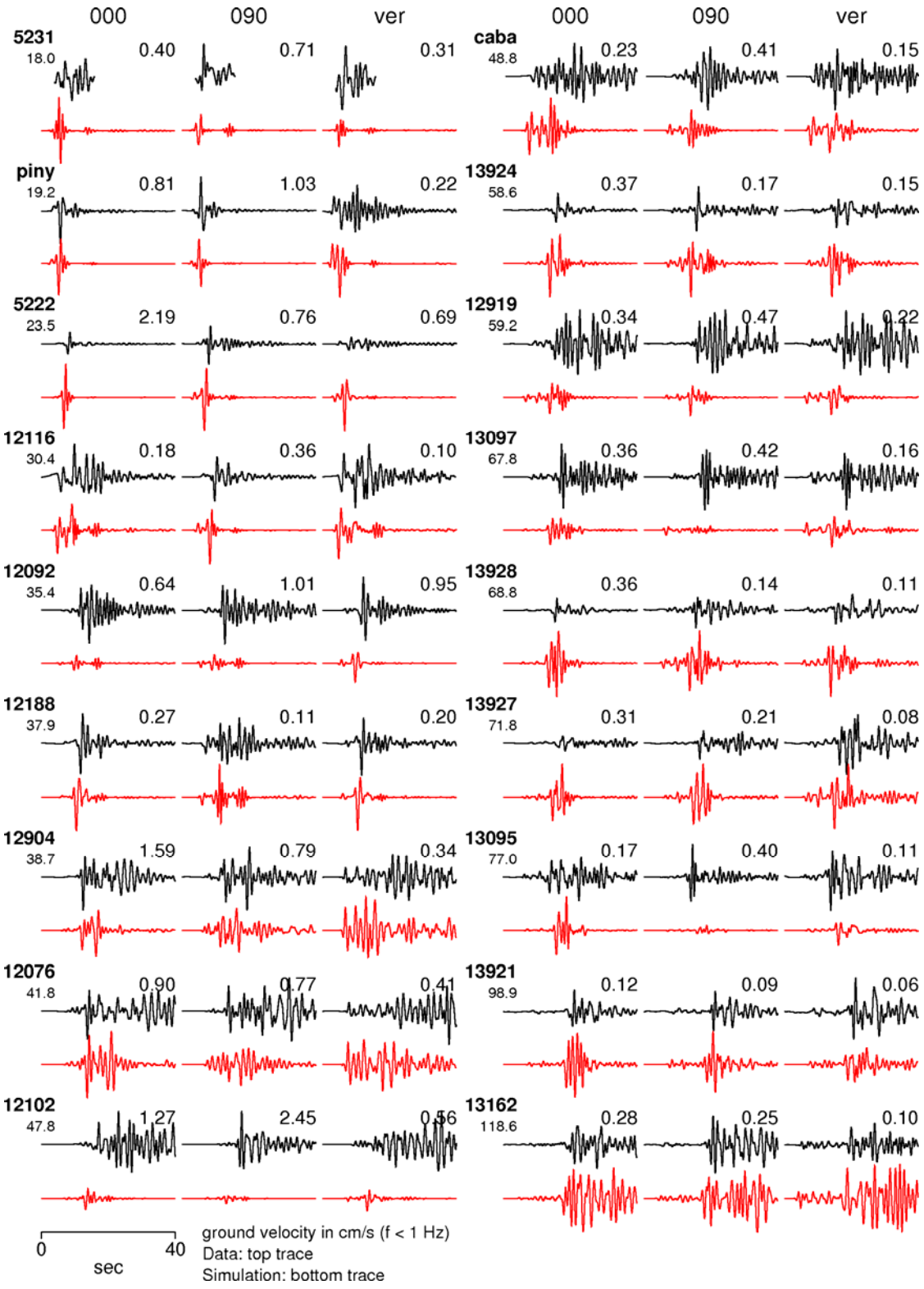

Figure 13: Comparison of recorded (black) and simulated (red) three component ground velocity waveforms at 18 selected sites. Both recorded and simulated motions have been bandpass filtered between 0.2 and 1.0 Hz. Site names and closest distance are listed to the left of each set of traces. Each data/synthetic pair is scaled to the same peak amplitude value which is shown above the traces (in cm/s).